ACS Catalysis

Research Article

pubs.acs.org/acscatalysis

Cobalt-Catalyzed Fischer–Tropsch Synthesis: Chemical Nature of the Oxide Support as a Performance Descriptor

Gonzalo Prieto,*[,†,§] Mariele I. S. De Mello,[†,‡] Patricia Concepción,[†] Raúl Murciano,[†] Sibele B. C. Pergher,[‡] and Agustín Martínez*[,†]

[†]Instituto de Tecnología Química UPV-CSIC, Avda. de los Naranjos s/n, 46022 Valencia, Spain

[‡]Laboratory of Molecular Sieves-LABPEMOL, Institute of Chemistry, Federal University of Rio Grande do Norte, Av. Senador Salgado Filho 3000, Lagoa Nova, Natal, Rio Grande do Norte 59072-970, Brazil

Supporting Information

ABSTRACT: The effect of the chemical nature of the oxide support on the performance of cobalt Fischer–Tropsch catalysts is investigated. A series of supports is synthesized via monolayer coverage of porous γ-Al_2O_3 with various oxides representative of a wide range of Lewis acid–base character, as quantified by UV–vis spectroscopy coupled to alizarin adsorption. Incorporation of cobalt (20 wt %) results in model catalysts with identical porosities and similar Co particle sizes (>10 nm), allowing the study of support effects without overlap from diffusional or particle size factors. Under realistic reaction conditions, the initial TOF scales with the acidity of the oxide support, whereas the cobalt time yield and selectivity to industrially relevant C_{13+} hydrocarbons show a volcano dependence, with a maximum at an intermediate acid–base character. As inferred from in situ CO-FTIR, "selective" blockage of a few cobalt sites, though crucial for CO hydrogenation, by atoms from basic oxides and "unselective" site blockage via decoration of Co nanoparticles (strong metal–support interaction) with acidic, reducible oxides cause a decrease in reaction rate for supports with pronounced alkaline and acidic character, respectively. The extent of secondary isomerization reactions of α-olefin products, of relevance for chain reinsertion processes and product selectivity, also correlates with the support acidity. For a TiO_x/Al_2O_3 as support, a remarkable C_{13+} productivity exceeding 0.09 $mol_C\ g_{Co}^{-1}\ h^{-1}$ is achieved, owing to the combination of optimal activity and selectivity. These results provide a unifying view of the support effects over a considerably broad study space and delineate a blueprint toward advanced Fischer–Tropsch catalysts.

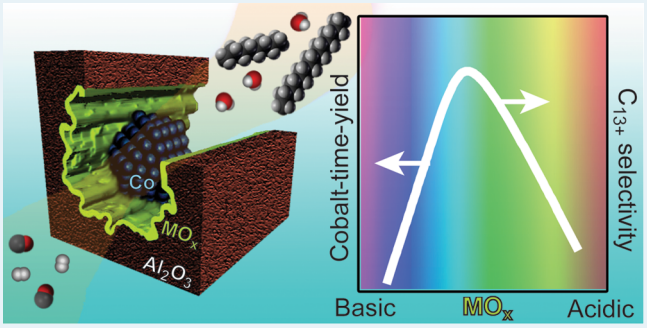

KEYWORDS: *Fischer–Tropsch synthesis, model catalysts, support effects, Lewis acidity, structure–performance relationships, turnover frequency, CO-FTIR spectroscopy*

INTRODUCTION

Gas to liquid (GTL)[1,2] and biomass to liquid (BTL)[3,4] processes based on the Fischer–Tropsch synthesis (FTS) of hydrocarbons from synthesis gas (syngas, CO + H_2) stand out as catalytic routes to convert oil-alternative carbon resources such as (stranded) natural gas, shale gas, or lignocellulosic biomass into clean liquid fuels and commodity chemicals. Cobalt nanoparticles supported on porous carriers, often containing minute amounts of reduction promoters such as Re, Ru, and Pt, are the catalysts of choice to maximize the yield to long-chain hydrocarbons, precursors of premium jet and diesel fuels and specialty lubricants.[5−7]

In recent years, the rising economic interest in FTS has triggered a great deal of research efforts committed to understanding the fundamental aspects of supported Co catalysts. Such an understanding represents an essential step toward the design and synthesis of catalysts with enhanced activity and selectivity toward long-chain hydrocarbons as well as extended lifetimes, as a means to improve the efficiency and reduce the carbon footprint of the process. Much of the earlier work has focused on the catalytically active Co nanoparticles. The synthesis and characterization of defined model catalysts have provided valuable insight into the effect of the Co particle size,[8−11] crystallographic structure,[12,13] and thermal history[14] as well as the role of metal promoters[15−17] on the performance.

The support material is also an essential component of Co-based FTS catalysts. It provides mechanical integrity and stabilizes the dispersed Co crystallites. A wide range of porous materials have been explored as carriers, including (mesostructured) SiO_2, Al_2O_3, and TiO_2,[5] mixed oxides,[18] zeolites,[19−21] SiC,[22] and carbon nanostructures.[8,23] Owing to their combination of suitable porosity, mechanical properties, and adequate stability under the hydrothermal conditions encountered in the FTS, the surface-modified SiO_2, Al_2O_3, and TiO_2

Received: January 13, 2015
Revised: April 16, 2015
Published: April 20, 2015

DOI: 10.1021/acscatal.5b00057
ACS Catal. 2015, 5, 3323−3335

have been primarily employed as support materials in technical Co catalysts. Currently, significant progress in materials synthesis has enabled the large-scale production of nanocrystalline, highly porous oxide materials in a great diversity of compositions.[24] This widens the array of materials which can be potentially considered as catalyst supports in a broad range of processes.

For Co-based FTS catalysts, earlier studies investigated the influence of the chemical nature of the oxide support material on the catalytic performance. Reuel and Bartholomew[25] found a decline in the catalytic activity per surface Co atom (or turnover frequency, TOF) in the order $Co/TiO_2 > Co/SiO_2 > Co/Al_2O_3 > Co/MgO$. A marked support effect on the hydrocarbon selectivity pattern was reported by Borg et al.[26] for similarly sized Co nanoparticles loaded on different Al_2O_3 allotropes. Likewise, the use of low-surface-area Nb_2O_5 as support was found by Schmal and co-workers to increase the selectivity to long-chain hydrocarbons in comparison to catalysts loaded on high-surface-area Al_2O_3 carriers.[27] Conversely, Iglesia and co-workers reported an insignificant support effect on the specific activity and selectivity for catalysts supported on SiO_2, Al_2O_3, TiO_2, and $MgCr_2O_4$.[28] The role of alkali-metal and rare-earth-metal oxides has also been a matter of study. For $CoRu/Al_2O_3$ catalysts, Takahashi et al.[29] found the modification of the Al_2O_3 carrier with rare-earth-metal oxides to have a positive impact on both the activity and the selectivity to heavy hydrocarbons. This is in contrast with the observation by Bertole et al.[30] of a notoriously detrimental effect of YO_x on the catalytic performance of $CoRe/Al_2O_3$ and $CoRe/TiO_2$ catalysts. Therefore, in spite of its scientific and technological significance, the impact of the chemical nature of the oxide support material on the catalytic performance is not yet fully understood, and seemingly contradictory conclusions are found in earlier literature.

In light of more recent insights, two main factors might be postulated to have contributed to the apparent discrepancies found in earlier studies. They both relate to the great variability of intrinsic textural properties commonly encountered among the different oxides explored as support materials. On one hand, dissimilar porosities are known to affect the rate of intrapellet diffusion of reactants and products, which has been shown to be relevant for both the activity and selectivity under standard operating conditions.[31−33] On the other hand, the common practice of applying a given cobalt weight loading onto supports with notably different specific surface areas often results in catalysts displaying markedly different metal dispersions. This is in turn expected to translate into activity (and selectivity) differences owing to particle size effects, which are known to set in for metal nanoparticles smaller than 8−10 nm.[8−10] Incomplete reduction of very small Co oxide nanocrystals is also known to lead to low activities and abnormally high methane selectivities.[34] Hence, unequivocally establishing the intrinsic impact of the chemical nature of the support material on the catalytic performance requires decoupling this effect from other influential factors through precise control of parameters such as support texture, extent of Co reduction, and particle size.

Here we investigate the effect of the acid−base character of the oxide support material on the performance of Co-based FTS catalysts under realistic reaction conditions. To ensure uniform textural properties irrespective of the surface composition, a series of support materials were synthesized by coating a common γ-Al_2O_3 porous carrier with a monolayer content of various transition-metal and lanthanide oxides spanning a wide range of acid−base character. These supports were employed to synthesize Ru-promoted Co catalysts with similar metal dispersion and high reducibility. The set of model catalysts enables a systematic study of intrinsic support effects on performance without overlap from diffusional or metal particle size/reducibility factors.

EXPERIMENTAL SECTION

Synthesis of MO_x@Al_2O_3 Supports. Several metal oxides MO_x (M = Sm, Y, Ta, Ti, W) were deposited on the surface of a high-surface-area γ-Al_2O_3 carrier. Monolayer (ML) coverages of the alumina surface by the metal oxide promoter (4.0−5.0 atoms nm^{-2}) were targeted. γ-Al_2O_3 was obtained by calcination of high-purity pseudoboehmite (Pural SB, Sasol) at 773 K for 10 h. Ta, Ti, Y, and W oxides were incorporated by impregnation of the dried Al_2O_3 substrate with alcoholic solutions of organometallic precursors (in excess to the pore volume) under a protective dry N_2 atmosphere.[35] In the case of SmO_x, an aqueous solution of $Sm(NO_3)_3$ was employed in the impregnation step (see the Supporting Information for details). The impregnated solids were dried at 333 K and calcined in a flow of air at 773 K for 3 h (heating rate 3 K min^{-1}, GHSV = 20 cm^3 g^{-1} min^{-1}). The resulting support materials are labeled as MO_x@AO, where MO_x denotes the oxide coating and AO stands for aluminum oxide. Accordingly, the uncoated γ-Al_2O_3 support is designated as AO.

Synthesis of $CoRu/MO_x@Al_2O_3$ Catalysts. Catalysts were prepared by impregnation of the predried support materials with an aqueous solution containing the required amounts of $Co(NO_3)_2{\cdot}6H_2O$ and ruthenium(III) nitrosyl nitrate precursors to achieve nominal Co and Ru loadings of 20 and 0.5 wt %, respectively. After impregnation, the solids were dried at 373 K and calcined at 573 K for 3 h in a flow of air (1 K min^{-1}). The catalysts are denoted as $CoRu/MO_x$@AO.

Characterization Methods. Chemical analysis was performed by ICP-OES in a Varian 715-ES ICP-optical emission spectrometer after dissolving the samples in a $HNO_3/HF/HCl$ solution (1/1/3 volume ratio). Due to incomplete dissolution in acids, the lanthanide content in YO_x@AO was evaluated by X-ray fluorescence spectroscopy (XRF) using a Philips MiniPal 25 fm setup. X-ray diffraction (XRD) patterns were recorded with a Philips X'pert diffractometer using monochromated Cu Kα radiation. The N_2 adsorption isotherms were measured with Micromeritics ASAP 2000 equipment after degassing the samples (ca. 200 mg) at 673 K for 24 h. Pore size distributions and average pore diameters were derived by applying the BJH model to the adsorption branch. The acid−base properties of the $MO_x@Al_2O_3$ supports were studied by DR UV−vis spectroscopy coupled with adsorption of alizarin (1,2-dihydroxy-9,10-anthracenedione).[36] The dried $MO_x@Al_2O_3$ solids were suspended in an ethanolic solution of alizarin (Aldrich). Then the solids were filtered, washed with ethanol, and dried under vacuum and the UV−vis spectra recorded in a Cary 5 spectrometer. The position of the IMCT band for adsorbed alizarin was determined via a first-derivative algorithm with the Peak Analyzer tool of the Origin Pro software package.

H_2 temperature-programmed reduction (H_2-TPR) profiles were recorded with a Micromeritics Autochem 2910 apparatus under a flow of 10 vol % H_2/Ar using a heating rate of 10 K min^{-1}. A downstream 2-propanol/N_2(l) trap (193 K) was used to retain the generated water. Solids containing basic YO_x or SmO_x oxides were previously submitted to in situ decarbon-

DOI: 10.1021/acscatal.5b00057
ACS Catal. 2015, 5, 3323−3335

Table 1. Physicochemical Properties of Oxide Support Materials

	composition		textural property				
support	M (wt %)	δ[a] (atoms nm^{-2})	BET[b] (m^2 g^{-1})	V_p[c] (cm^3 g^{-1})	V_p[d] (cm^3 $g_{Al_2O_3}^{-1}$)	PD[e] (cm^3 g^{-1})	acid–base character η[f] (eV)
AO			205	0.52	0.52	8.9	2.49
SmO_x@AO	18.7[g]	4.7[g]	155	0.39	0.50	7.9	2.38
YO_x@AO	12.1[h]	4.7[h]	174	0.44	0.52	7.9	2.46
TiO_x@AO	6.2	4.2	192	0.46	0.51	8.0	2.50
TaO_x@AO	23.5	5.3	176	0.34	0.47	7.0	2.53
WO_x@AO	24.0	5.5	178	0.37	0.53	7.0	2.61

[a]Surface coverage of the alumina surface with M atoms. [b]BET = specific surface area. [c]Total specific pore volume. [d]Total specific pore volume expressed per unit mass of Al_2O_3. [e]Average pore diameter. [f]Energy of intramolecular charge transfer (IMCT) band of adsorbed alizarin (see text). Standard error ($s/N^{1/2}$) <0.5%. [g]Nominal values. [h]Determined by X-ray fluorescence spectrometry.

ation in a flow of synthetic air at 873 K for 2 h. H_2 consumption was monitored in a calibrated TCD detector. For transmission electron microscopy (TEM), catalysts were ex situ reduced under a flow of H_2 at 673 K, passivated at room temperature under a flow of 0.5% O_2/Ar, and embedded in a resin; slices of the resin of ca. 40 nm thickness were obtained with a microtome and mounted on a carbon-coated Cu TEM grid for observation. Cobalt particle sizes were corrected for the presence of a 3 nm thick CoO passivation outlayer. The metal surface area in the reduced catalysts was determined by H_2 chemisorption at 423 K with ASAP 2010C Micromeritics equipment by extrapolating the total gas uptakes to zero pressure.[37] Prior to adsorption, the samples (ca. 0.5 g) were pretreated under flowing He at 393 K for 1 h and reduced under a flow of H_2 at 673 K. The surface atomic ratio H/Co = 1 was assumed.

XPS spectra were recorded with a SPECS spectrometer equipped with a Phoibos 150 MCD-9 detector using a nonmonochromatic X-ray source (Al and Mg) operating at 200 W. Calcined samples were pressed into small disks and evacuated in the prechamber of the spectrometer at 10^{-9} mbar. Previously reduced and passivated samples were also investigated after in situ reduction under flowing H_2 (673 K, 2 h) and reaction under flowing syngas (H_2/CO = 2, 493 K, 4 h) in a dedicated high-temperature cell attached to the spectrometer. In situ CO-FTIR experiments were performed with a Bruker Vertex70 spectrometer using a homemade quartz cell fitted with KRS-5 windows and connected to a vacuum dosing system. Passivated catalysts were pressed into self-supported wafers (5–10 mg cm^{-2}) and reduced in the IR cell under a flow of H_2 at 673 K for 2 h. Then, the samples were outgassed under vacuum (ca. 10^{-5} mbar) at 723 K (50 K above the reduction temperature) to allow for the displacement of any H_2 adsorbed on the metal surface and then cooled to room temperature under vacuum. For CO adsorption experiments, CO was added at increasing pressure (0.4–8.5 mbar) and the IR spectrum recorded after each dosage. For in situ IR experiments under syngas conversion conditions, the reduced samples were exposed to a flow (50 cm^3 min^{-1}) of syngas at room temperature for 1 h to ensure a homogeneous atmosphere in the cell. Then, the temperature was increased stepwise from room temperature to 493 K and maintained at this temperature for 4 h. The IR spectra were recorded after 10 min at each temperature and after 10, 60, 120, 210, and 240 min on-stream at the final temperature (493 K). After reaction, the catalysts were submitted to either evacuation or a 50% H_2/Ar flow (50 cm^3 min^{-1}) at 493 K for 1 h to investigate the stability of the adsorbed CO–Co species.

Catalysis. Catalytic experiments were performed in a fixed-bed 310 stainless steel reactor loaded with ca. 1.5 g of catalyst (0.25–0.42 mm pellet size) diluted with SiC granules to attain a constant bed volume of 6.4 cm^3. Prior to reaction the catalyst was reduced in situ under a flow of H_2 at 673 K for 10 h (1 K min^{-1}). The reaction was carried out at 493 K and 20 bar using a feed with the molar composition 30% CO/60% H_2/10% Ar (Ar as GC standard). The stream leaving the reactor was depressurized and periodically analyzed on line with a GC (Varian 3800) equipped with TCD and FID detectors,[9] while liquid products were collected in high-pressure traps, weighed, diluted with CS_2, and analyzed offline. With this procedure, carbon mass balances amounted to 100 ± 2%. Product selectivities are reported on a carbon basis after 8 h on-stream after the gas space velocity (GHSV) was adjusted to achieve a CO conversion level of 40 ± 5% in the pseudo steady state.

Chain-growth probabilities for hydrocarbons with n carbon atoms were derived from the experimental product distributions using eq 1:[38]

$$\alpha_{C_n} = \frac{R_{prop,n}}{R_{prop,n} + R_{term,n}} = \frac{\sum_{i=n+1}^{\infty} F_i}{\sum_{i=n}^{\infty} F_i} \quad (1)$$

where R representd the rate of chain propagation (prop) or termination (term) of C_n* hydrocarbon species and F_i stands for the total molar flow of C_i hydrocarbon products.

RESULTS AND DISCUSSION

Physicochemical Properties of Support Materials. The metal contents, precursors, and synthesis conditions were adjusted to cover the surface of the Al_2O_3 substrate with a monolayer content of the MO_x oxides. For the series of investigated oxides, the theoretical monolayer coverage lies in the range of 4–5 atoms nm^{-2}.[35] Table 1 gives the metal contents and textural properties for the resulting MO_x@AO supports. The experimental MO_x coverages are in agreement with the theoretical values, with deviations of <10%. No X-ray diffractions other than those corresponding to the γ-Al_2O_3 substrate were detected (Figure S1 in the Supporting Information), indicative of the absence of three-dimensional crystallites of the metal and lanthanide oxides deposited. Quantitative analysis of XPS spectra for the calcined MO_x@AO support materials was in fair correspondence (deviations of <15%) with predictions by the Kerkhof–Moulijn model[39] for a monolayer dispersion of the supported oxides on the high-surface-area Al_2O_3 carrier (Figure S2 in the Supporting Information). N_2 physisorption revealed a decrease in the specific BET surface area and pore volume upon incorporation of the MO_x species on the Al_2O_3 carrier. This is mainly the

DOI: 10.1021/acscatal.5b00057
ACS Catal. 2015, 5, 3323–3335

Table 2. Physicochemical Properties of CoRu/MO_x@Al_2O_3 Catalysts

	metal content		textural property		metal dispersion			
catalyst	Co (wt %)	Ru (wt %)	BET[a] (m^2 $g_{Al_2O_3}^{-1}$)	V_p[b] (cm^3 $g_{Al_2O_3}^{-1}$)	$d(Co_3O_4)_{XRD}$[c] (nm)	$d(Co)_{TEM}$[d] (nm)	H_2 uptake[e] (μmol g^{-1})	$d(Co)_H$[f] (nm)
CoRu/AO	22.1	0.3	260	0.52	17.3		144	12.5
CoRu/SmO_x@AO	21.8	0.3	292	0.49	12.7	13.6	126	14.1
CoRu/YO_x@AO	21.4	0.2	271	0.45	10.5		162	10.8
CoRu/TiO_x@AO	22.8	0.2	261	0.44	13.3	13.0	132	14.1
CoRu/TaO_x@AO	22.1	0.2	265	0.53	17.4		124	14.6
CoRu/WO_x@AO	19.9	0.2	258	0.47	13.1	16.3	41	39.7

[a]BET = specific surface area expressed per unit mass of Al_2O_3. [b]Total specific pore volume expressed per unit mass of Al_2O_3. [c]Co_3O_4 crystallite size after air calcination. [d]Surface-averaged Co particle size distribution as determined by TEM on the reduced and passivated catalysts. [e]Total hydrogen uptake as determined after in situ reduction. [f]Apparent Co average particle size as derived from the total H_2 chemisorption uptake.

result of the increment in the density of the solids after oxide loading. When they were normalized by the mass of Al_2O_3, the specific pore volumes for all MO_x@AO samples were very similar (0.51 ± 0.02 cm^3 $g_{Al_2O_3}^{-1}$) to that of the pristine γ-Al_2O_3, showing that the incorporation of MO_x species did not cause any appreciable pore plugging. All MO_x@AO solids displayed nearly identical average pore sizes of 7.5 ± 0.5 nm: i.e., 10−20% lower than that of the pristine γ-Al_2O_3 carrier. Jointly, these results indicate that the MO_x oxides were deposited as a nanometer-thin 2D layer, preserving the porosity of the γ-Al_2O_3 substrate.

Essential for the purpose of this study is an adequate description of the acid−base character of the MO_x@AO support materials. Earlier, Yoon and co-workers reported that the lowest intramolecular charge transfer energy E(IMCT) of adsorbed alizarin (1,2-dihydroxy-9,10-anthracenedione) is a very sensitive and universal measure of the surface Lewis acid−base character of metal chalcogenides.[36] Here we have adopted this method to establish a quantitative ranking of surface acidity for the MO_x@AO supports. After equilibrium adsorption of the probe molecule, the UV−vis spectra of the solids displayed a characteristic band in the energy range of 1.5−3.5 eV, corresponding to the E(IMCT) value from the cathecol moiety to the aromatic system of the alizarin molecule (Figure S3 in the Supporting Information). Table 1 gives the peaking energies for this band (hereafter referred to as the η spectroscopic parameter) for the series of MO_x@AO supports. It ranges from 2.38 eV, corresponding to the marked basic character of SmO_x@AO, to 2.61 eV for an oxide with a strong Lewis acid character such as WO_x@AO. The remaining solids, showing intermediate η values, are also ranked according to their relative acid−base nature. Direct comparison of the η values determined for the series of MO_x@AO samples with the theoretical acidity for the bulk M_yO_z oxide counterparts (Figure S4 in the Supporting Information) corroborates that the acid−base ranking established for the monolayer oxides adequately represents the relative acid−base character of the corresponding bulk oxides.

Overall, these physicochemical characterizations show that the series of MO_x@AO support materials display comparable porosities irrespective of the nature of the MO_x species, while they span a broad range of surface acid−base character, representative of a diversity of metal and lanthanide oxides.

Physicochemical Properties of CoRu/MO_x@AO Catalysts. Surface Co^0 atoms are consensually known to be the active species under standard Fischer−Tropsch reaction conditions. Hence, cobalt dispersion and reducibility are metal-related parameters determinant for the catalytic performance. Table 2 summarizes the metal content, textural properties, and metal dispersion determined for the set of CoRu/MO_x@AO catalysts. After air calcination, cobalt contents ranged from 19.9 to 22.8 wt %, corresponding to surface-specific loadings of 11.9 ± 0.9 atoms of Co nm^{-2}. For ruthenium, loadings systematically lower than the nominal content of 0.5 wt % were determined in the calcined samples, which is ascribed to formation and issuance of volatile RuO_x species to the gas flow during the calcination treatment.[33] After cobalt loading, the accessible pore volume was 0.48 ± 0.04 cm^3 $g_{Al_2O_3}^{-1}$ for all catalysts. The ca. 5−10% pore volume decrease with respect to the MO_x@AO support materials agrees reasonably well with the volume expected for the Co_3O_4 crystallites, indicative of the successful incorporation of cobalt within the porosity of the support without any significant pore blockage.

The spinel Co_3O_4 was the only crystalline metal phase detected by X-ray diffraction in the calcined catalysts (not shown). Co_3O_4 crystallite sizes in the range of 11−17 nm were determined from line broadening analysis (Table 2). After reduction, the Co metal particle size was studied by TEM in selected catalysts synthesized on supports representative of the entire range of acid−base character. As shown in Figure 1, low-magnification imaging of catalyst cross sections revealed clustering of the Co nanoparticles in high-metal-density domains (50−300 nm), particularly for CoRu/SmO_x@AO and CoRu/TiO_x@AO. Such nonuniform metal distributions are found rather often in supported catalysts prepared by impregnation of nitrate metal precursors on typical oxide supports.[40,41] In view of the corresponding particle size histograms, the large majority of the Co nanoparticles showed sizes exceeding 10 nm: i.e., the range where no particle size effects are expected on the TOF under FTS conditions.[8,9] As given in Table 2, TEM-derived average Co metal particle sizes in the range 13.0−16.3 nm were obtained for the studied samples.

The reducibility of the CoRu/MO_x@AO catalysts was studied with H_2-TPR. Figure 2 depicts the reduction profiles, along with those for the corresponding MO_x@AO support materials. Among the supports, only WO_x@AO showed a measurable reduction feature at temperatures above 1100 K. The remaining MO_x species showed no detectable H_2 consumption in the examined temperature range, indicative of a low reducibility. In the case of the CoRu/MO_x@AO catalysts, two main reduction features peaking in the range 467−690 K were detected, ascribed to the stepwise reduction of the supported Co_3O_4 nanocrystals to metallic Co^0.[14] For CoRu/WO_x@AO, these signals appeared partially overlapped,

DOI: 10.1021/acscatal.5b00057
ACS Catal. 2015, 5, 3323−3335

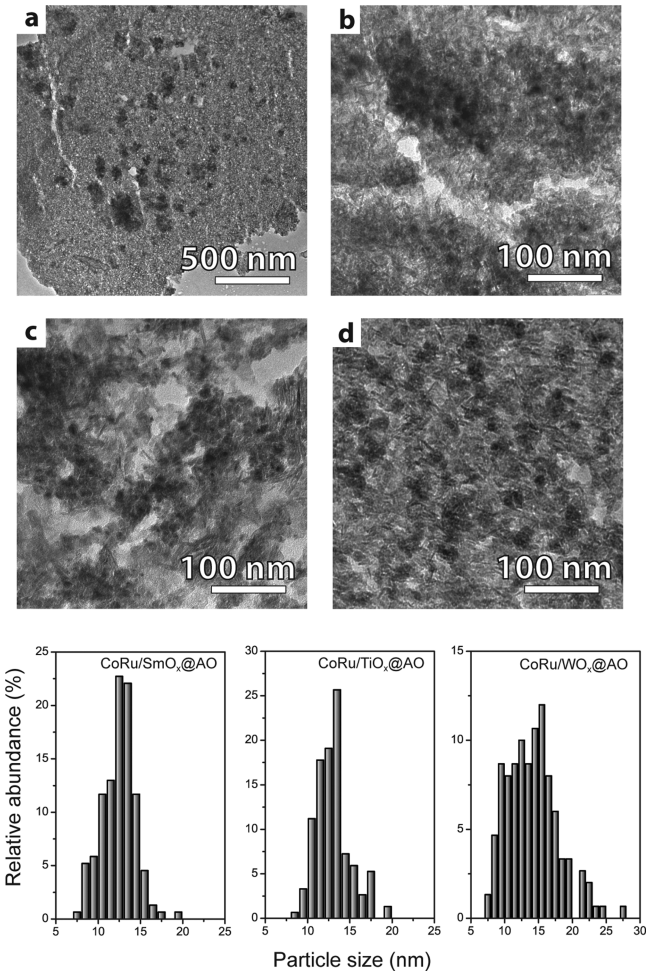

Figure 1. Bright-field TEM micrographs of CoRu/SmO_x@AO (a, b), CoRu/TiO_x@AO (c), and CoRu/WO_x@AO (d) after reduction (H_2 flow, 673 K, 10 h) and passivation. The corresponding Co particle size histograms are shown at the bottom of the figure.

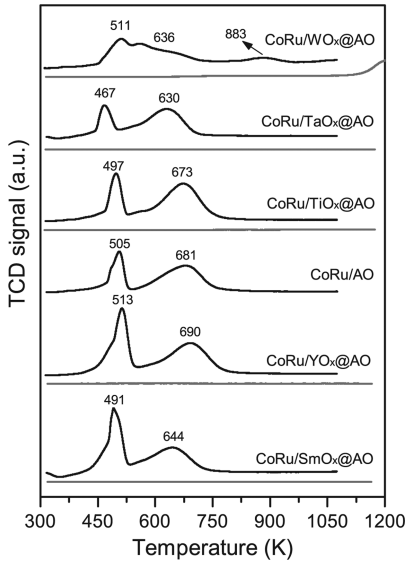

Figure 2. H_2-temperature-programmed reduction profiles for MO_x@AO support materials (gray lines) and the corresponding CoRu/MO_x@AO catalysts (black lines).

resulting in a broad band. In view of these H_2-TPR profiles, it is sensible to assume in all cases the quantitative reduction of the Ru and Co species after the reduction treatment preceding catalysis (673 K, 10 h in pure H_2). For CoRu/WO_x@AO, a weak reduction feature peaking at 883 K is ascribed to the partial reduction of WO_x species, which appears shifted to lower temperatures in comparison to the WO_x@AO support, likely due to the capacity of Co^0 and Ru^0 species to supply dissociated hydrogen species via spillover at lower temperatures.

The exposed metal surface area after catalyst reduction was determined by H_2 chemisorption. As given in Table 2, relatively high H_2 uptakes in the range of 124−162 μmol g^{-1} were determined for most catalysts. The amount of adsorbed H_2 translated into apparent Co^0 particle sizes in the range 11−15 nm, in reasonably good agreement with TEM results. Together, these results indicate the effective exposure of the surface of the Co^0 nanoparticles and discard any extensive decoration by MO_x species. In contrast, a notably lower H_2 uptake of 41 μmol g^{-1} was measured for CoRu/WO_x@AO, which corresponds to a specific metal surface area of ca. 40% that was expected on the basis of the Co particle size determined by TEM. In this case, partial coverage of the metal surface by WO_x species is inferred. The migration of MO_x patches on the surface of the metal nanoparticles upon catalyst reduction, the so-called strong metal−support interaction (SMSI), is a well-documented phenomenon for cobalt catalysts supported on partially reducible oxides.[27,42] Within the series of materials investigated here, SMSI is expected to be increasingly favored on increasing the acidic nature of the support, given that stronger Lewis acid oxides are generally more reducible, as they bear electron-withdrawing metal cations in high oxidation states. This was supported by our in situ XPS analysis of selected catalysts at different stages, which confirmed the partial reduction of WO_x species during catalyst activation (Figure S5 in the Supporting Information). For catalysts supported on other relatively reducible oxides such as TaO_x@AO and TiO_x@AO, the metal surface areas determined by H_2 chemisorption after reduction indicate that SMSI effects, if present, must have occurred to a minor extent. In the case of Co nanoparticles deposited on the most reducible WO_x@AO oxide support, our results clearly indicate that a significant fraction of the Co surface is covered by WO_x species after reduction.

It ensues from these results that the series of CoRu/MO_x@AO catalysts display fully reducible, similarly sized Co nanoparticles in the size range >10 nm, where no particle size effects on activity are expected. These features make the set of materials an ideal platform to investigate intrinsic support effects on the catalytic performance without overlap from concomitant factors associated with the metallic nanoparticles: i.e., reduction extent and particle size.

Catalytic Properties. *Fischer−Tropsch Synthesis.* The catalytic properties of the series of CoRu/MO_x@AO catalysts were evaluated under industrially significant reaction conditions. In Figure 3, relevant performance parameters are depicted as a function of the acid−base character of the MO_x underlying oxide support, given by the spectroscopic parameter η. The initial (extrapolated to zero time-on-stream) turnover frequency (TOF) increased linearly with increasing η (Figure 3a). Catalysts supported on more basic oxides showed a notably lower metal surface-specific CO conversion rate in comparison to materials with Co nanoparticles deposited on acidic oxides. For example, the TOF was ca. 1 order of

DOI: 10.1021/acscatal.5b00057
ACS Catal. 2015, 5, 3323−3335

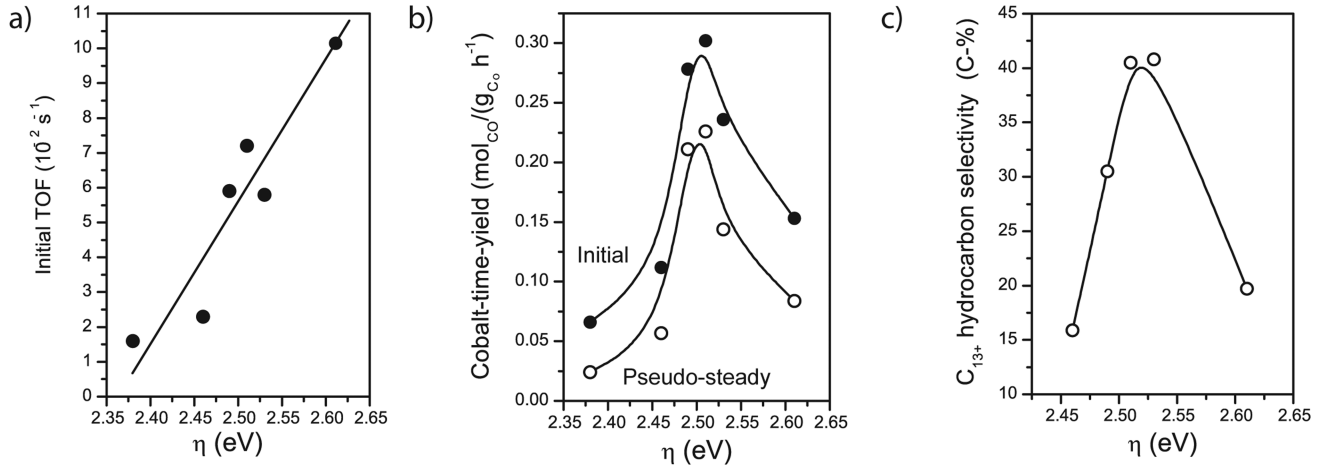

Figure 3. Evolution of (a) the initial turnover frequency (per surface metal atom), (b) the initial (full symbols) and pseudosteady (open symbols) cobalt time yield, and (c) the C_{13+} hydrocarbon selectivity obtained with CoRu/MO_x@AO catalysts as a function of the acid−base character of the support material, represented by the spectroscopic parameter η (see text). Reaction conditions: T = 493 K, P = 20 bar, initial GHSV = 6.9 L_{syngas} g_{cat}^{-1} h^{-1}. Data included in (c) correspond to the steady state after adjusting the gas space velocity to achieve a CO conversion level of 40 ± 5% in all cases. Data for CoRu/SmO_x@AO have not been included in this panel, as the intrinsic lower activity of this catalyst prevented achieving the mentioned CO conversion level. Lines serve as guides to the eye.

magnitude higher for CoRu/WO_x@AO than for CoRu/SmO_x@AO. Hence, in spite of the fact that partial coverage of the cobalt nanoparticles by WO_x species upon catalyst reduction decreases the exposed metal surface area, those surface Co atoms which remain available for catalysis show the highest intrinsic activity. It has been previously proposed that direct contact with Lewis acid oxides can promote CO hydrogenation on cobalt[43] and other metals.[44] Working with 2D "inverse model catalysts", comprising metal oxide patches decorating the surface of metal single crystals, Somorjai and co-workers[45] found a quantitative relationship between the ability of the metal oxides to promote CO hydrogenation and their Lewis acid character. Our results on porous model catalysts exposed to industrially relevant Fischer−Tropsch reaction conditions are in agreement with these previous observations and indicate a direct relationship between the Lewis acid−base character of the support material and the intrinsic catalytic activity of the surface-exposed cobalt atoms.

The metal-specific catalytic activity (cobalt time yield, CTY) showed a volcano-type dependence with η (Figure 3b). The trends were essentially identical, whether in the initial or pseudo steady reaction stages. Considering the evolution of TOF with η shown in Figure 3a, the existence of a maximum in CTY for intermediate values of η is interpreted as the result of a compromise between the intrinsic catalytic activity of the exposed metal sites, which decreases for lower η values (more basic supports), and the cobalt surface area effectively available for catalysis, which is reduced for high values of η as a result of the partial coverage of the Co nanoparticles by oxide patches. The maximum metal-specific catalytic activity was achieved with CoRu/TiO_x@AO (η = 2.50 eV), which reached a remarkable cobalt time yield of 0.23 mol_{CO} g_{Co}^{-1} h^{-1} in the steady state, an activity which stands out among literature values for Co-based catalysts (Figure S6 in the Supporting Information).

Beyond activity, the catalytic selectivity is a key parameter, determinant for the overall economy and environmental impact of the process. Particularly desirable is maximizing the production of long-chain hydrocarbons in the distillate and wax fractions (C_{13+}) which can be upgraded downstream into synthetic liquid fuels.[7] The product selectivities were determined for the series of CoRu/MO_x@AO catalysts in the steady state, at a conversion level of ca. 40% (Table S1 in the Supporting Information). CO_2 selectivities were low (≤0.8%) in all cases, indicating a modest activity for the water-gas shift reaction, as is characteristic for Co-based catalysts under standard reaction conditions. Most notably, significant differences in the selectivity to different hydrocarbon fractions were apparent, which showed a marked dependence on the acid−base character of the oxide support. CoRu/Al_2O_3 and those catalysts supported on other oxides with an intermediate acid−base character (η = 2.49−2.53 eV) showed comparable methane selectivities in the range 14.9 ± 0.5%. The selectivity to methane decreased significantly to ca. 10% for a more basic oxide support such as YO_x@AO and increased to ca. 20% for a support with marked acidic character such as WO_x@AO. The selectivity to the desired fraction of C_{13+} hydrocarbons showed a volcano dependence with η (Figure 3c), with a maximum exceeding 40% for catalysts supported on TiO_x@AO and TaO_x@AO. In contrast, on both sides of the apex, support materials with pronounced basic or acidic character resulted in poor C_{13+} selectivities in the range of 15−20%.

Owing to its combination of optimal CO conversion rate and C_{13+} selectivity, the catalyst supported on TiO_x@AO gave the highest productivity to the desired heavy hydrocarbon fraction, between 42% and 9-fold superior to those of any of the other investigated catalysts (Figure S7 in the Supporting Information). Previous studies have highlighted the benefits of TiO_2 supports to achieve high activity and selectivity to long-chain products with cobalt-based Fischer−Tropsch catalysts.[25,46,47] TiO_2 nanocrystals with a size of a few tens of nanometers, e.g. Evonik's P25 TiO_2, are commonly applied as supports. However, in its massive form, TiO_2 displays relatively low specific surface areas, generally <60 and <10 m^2 g^{-1} for anatase and rutile allotropes, respectively. This limits the Co loading that can be applied in Fischer−Tropsch catalyst formulations (generally <10 wt %) to maintain high metal dispersions. Our results demonstrate that covering a conventional high-surface-area Al_2O_3 carrier with a monolayer content of TiO_x species represents a simple, inexpensive, and effective approach to

DOI: 10.1021/acscatal.5b00057
ACS Catal. 2015, 5, 3323−3335

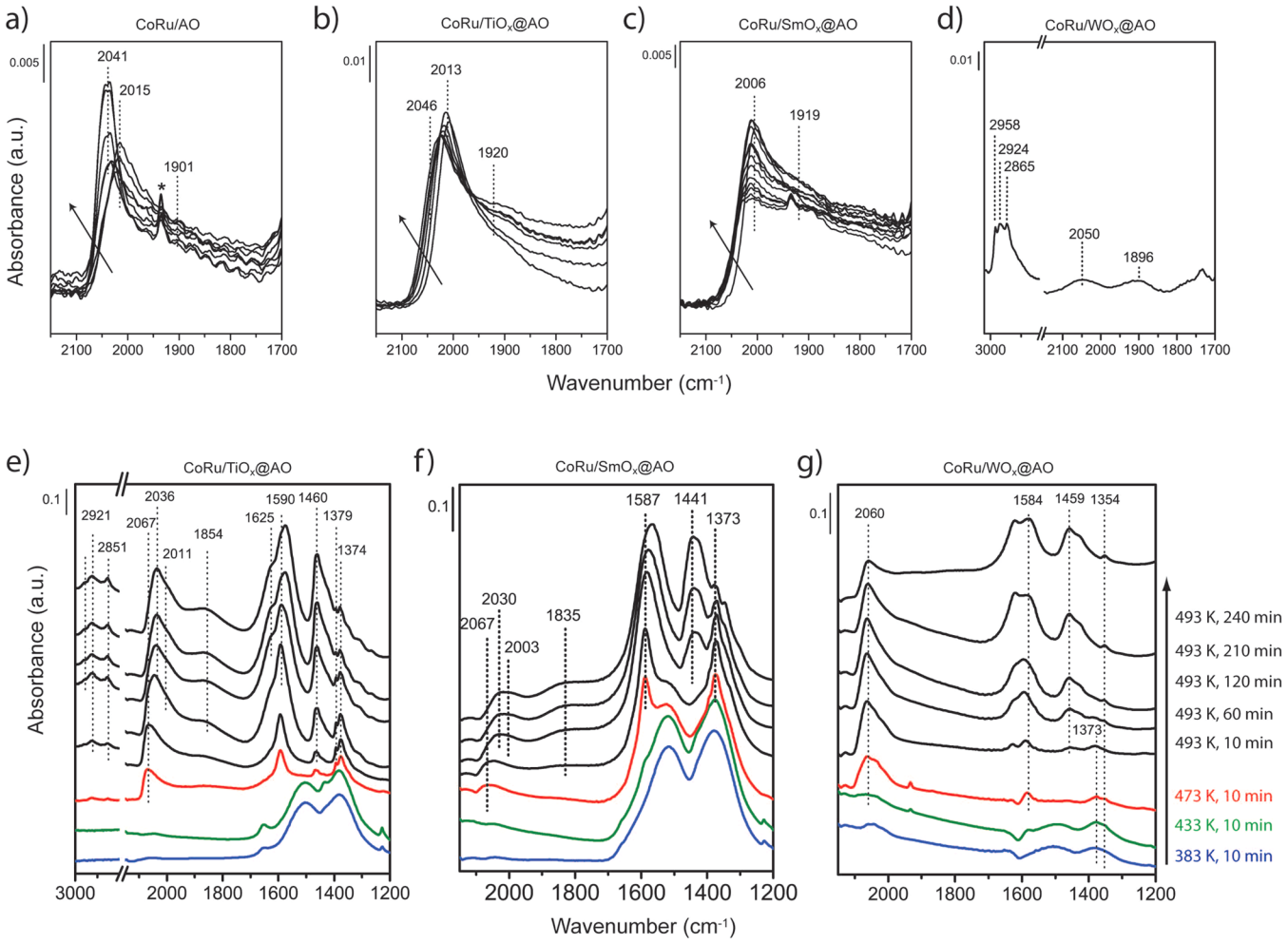

Figure 4. (a–d) Fourier transform infrared (FTIR) spectra after adsorption of CO at 298 K, with stepwise increasing dosages, on selected CoRu/MO_x@AO catalysts after reduction. The arrow indicates increasing CO dosage in the range 0.4–8.5 mbar. The sharp signal detected in some spectra at 1935 cm^{-1} (labeled with an asterisk) corresponds to a spike band; hence, it is not related to the sample. (e–g) In situ temperature- and time-resolved FTIR spectra of selected CoRu/MO_x@AO catalysts under a flow of synthesis gas (H_2/CO = 2) at P = 1 bar and T = 383–493 K.

combine the advantageous textural properties of a highly porous substrate with the optimal chemical characteristics of Ti oxides in high-Co-loading catalysts, leading to superior mass-specific productivities of long-chain hydrocarbons.

In Situ CO-FTIR Spectroscopy. CO-FTIR was applied to investigate the surface topology of Co nanoparticles deposited on selected oxide supports and their interaction with CO under reaction conditions. Figure 4 depicts the FTIR spectra recorded after stepwise dosage of CO on in situ reduced catalysts. For CoRu/AO (Figure 4a), cobalt carbonyl bands developed in the region 1800–2100 cm^{-1} upon admission of CO. A band at 2015 cm^{-1} ascribed to CO linearly adsorbed on coordinatively unsaturated (cus) Co sites[9,14] was detected at low CO doses. When the CO dosage was increased, the intensity of this band decreased while another band at 2041 cm^{-1} ascribed to CO linearly adsorbed on low-index Co facets[14,48] gradually developed. The interconversion of the two bands suggests a surface reconstruction upon CO adsorption and dissociation.[49] The occurrence of such CO-driven reconstruction of the cobalt surface is supported by the fact that the application of a second CO dosage cycle at room temperature, once full CO coverage was achieved during the first adsorption cycle and the adsorbed CO was subsequently removed via cell evacuation, did not reproduce the spectra recorded on the pristine metallic surface (Figure S8 in the Supporting Information). In addition, a broad band was observed at ca. 1901 cm^{-1}, which corresponds to CO adsorbed in a bridged configuration on Co terraces.[9,47] A similar result was observed for CoRu/TiO_x@AO (Figure 4b), which suggests an analogous metal surface topology in both catalysts.

In the case of CoRu/SmO_x@AO (Figure 4c), the single linear carbonyl band detected at low CO doses peaked at a significantly lower frequency (2006 cm^{-1}) in comparison to the previously discussed catalysts, indicating an increased electron back-donation from the d orbitals of the cus metal sites to the $2\pi^*$ orbital of CO.[50] For metal nanoparticles larger than 10 nm, such as those studied here, no perceivable influence of electron transfer phenomena from the underlying support on the electronic density of the surface metal atoms is expected. Likewise, large variations in the metal nanoparticle morphology, and thereby surface topology, are not likely for such particle sizes. Hence, we attribute this effect to the transfer of electronic density from Sm atoms, migrated from the support, to the surface Co sites. The induction of a CO tilted adsorption mode on Sm–Co pair sites would also result in lower CO vibration frequencies. While no significant blockage of the total cobalt surface area is observed, as judged from H_2 chemisorption results, a very low coverage of Sm atoms is expected to be

DOI: 10.1021/acscatal.5b00057
ACS Catal. 2015, 5, 3323–3335

sufficient to notably affect the CO−Co interaction. This has indeed been previously demonstrated by surface science studies of highly electron donating atoms on metallic surfaces, which additionally identified step-edge surface metal sites as the preferred sitting sites for the decorating atoms.[51,52] The development of higher frequency linear carbonyl bands with an increase in the CO dosage was significantly less marked in this case, suggestive of a lower extent of cobalt surface reconstruction in comparison to catalysts supported on Al_2O_3 and TiO_x@Al_2O_3 oxides, related to a lower ability of CoRu/SmO_x@AO to dissociate CO at room temperature. For these three catalysts, formation of carbonate species on the oxide supports was evidenced by the development of IR bands in the region 1200−1700 cm^{-1} at increasing CO coverages (Figure S9 in the Supporting Information).

No obvious signs of Co carbonyl bands were observed upon dosing CO at room temperature on the activated CoRu/WO_x@AO catalyst (Figure 4d). Remarkably, the presence of incipient bands peaking at 2958, 2924, and 2865 cm^{-1} of surface methyl ($-CH_3$) and methylene ($-CH_2-$) groups indicates that CO hydrogenation took place readily upon adsorption. The resulting C_xH_y species render the metallic surface blocked for further uptake of molecular CO. The detection of hydrogenated species strongly suggests that such higher activity is associated with the presence of H* species remaining on the catalyst surface after the reduction step, which are known to significantly lower the activation barriers for CO dissociation.[53−55] We ascribe the observation of this phenomenon only for this catalyst to the ability of partially reduced WO_x species to "store" and supply dissociated hydrogen via spillover to the vicinal Co sites.

Figure 4 also depicts the FTIR spectra recorded in situ during exposure of the reduced catalysts to a flow of syngas at increasing temperatures up to 493 K. Irrespective of the nature of the catalyst, no metal carbonyl bands were detected in the temperature range 383−433 K, showing that the metal surface remained covered by C* and O* species coming from CO dissociation, whereas CH_x and carbonate species were detected on the oxide support surface (broad intense bands in the 1600−1300 cm^{-1} IR region). Adsorption of molecular CO on the metal was restored at 473 K. For Co nanoparticles supported on TiO_x@AO and SmO_x@AO (Figure 4e,f), a right-skewed band peaking at 2067 cm^{-1} was observed at this temperature, whose frequency corresponds to CO linearly adsorbed on an extensively carburized cobalt surface.[47] Analysis of the 1300−1600 cm^{-1} spectral range indicates simultaneous replacement of carbonates by formate species on the surface of the oxide support, as a result of the increasing hydrogenation capacity of the catalyst on increasing the temperature. After the temperature was raised to 493 K and the catalysts exposed to FTS conditions for 1 h, the IR band for linear metal carbonyls experienced a significant red shift. The new band peaked at 2036 and 2030 cm^{-1} for CoRu/TiO_x@AO and CoRu/SmO_x@AO, respectively, indicating that carbidic surface species become hydrogenated and the fully metallic cobalt surface is restored at the FTS reaction temperature. A prominent shoulder at 2003 cm^{-1} was observed in the IR spectra of the "working" CoRu/SmO_x@AO catalyst, indicating the persistence of a fraction of Co sites with enhanced electronic density in this catalyst, also under reaction conditions. In addition, a broad band at 1830−1855 cm^{-1} developed for both catalysts, ascribed to bridged CO adsorption on cobalt terraces. As shown in Figure 4e for CoRu/TiO_x@AO, signs of Fischer−Tropsch activity at the reaction temperature of 493 K were evidenced by the development of bands at 2851 and 2921 cm^{-1}, which reveal the formation of C_{2+} hydrocarbon species. In addition, accumulation of carboxylate species on the oxide support was also evident in all cases from the time evolution of the characteristic bands in the 1200−1700 cm^{-1} spectral region. The later species were strongly adsorbed (the associated bands remained impervious to cell evacuation at 493 K).

CO-FTIR monitoring of CoRu/WO_x@AO under syngas conversion conditions (Figure 4g) revealed an analogous behavior, although two significant differences were observed in the Co carbonyl region. First, the band corresponding to CO linearly adsorbed on cobalt, which emerged at 473 K, peaked at 2060 cm^{-1} with a tail down to 1990 cm^{-1}, and did not suffer any appreciable shift on increasing the temperature up to 493 K or maintaining this reaction temperature for 4 h. It is therefore inferred that the cobalt surface does not exist in a carburized form at any temperature and therefore surface decarburization/reconstruction does not occur upon reaching the reaction temperature of 493 K. Again, this result points to a higher hydrogenation power for this catalyst, as discussed previously. Second, under reaction conditions, no obvious band was detected in the region of bridged cobalt carbonyls, showing that a large fraction of the cobalt terraces remains covered by WO_x species (SMSI) during catalysis.

The stability of different carbonyl species existing on the cobalt surface during catalysis was assessed by their susceptibility to hydrogenation (and evacuation) at the reaction temperature of 493 K. Figure 5 depicts the CO-FTIR spectra

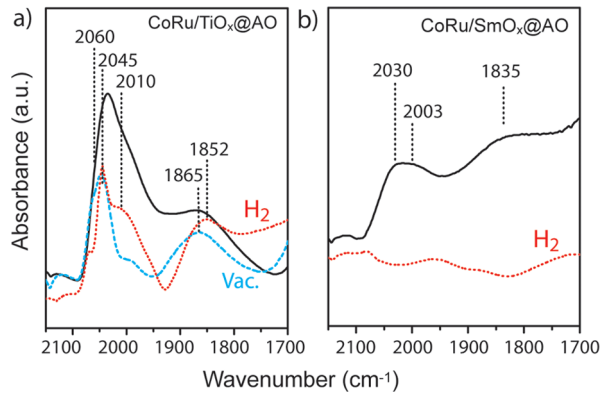

Figure 5. Susceptibility of cobalt-adsorbed CO species to evacuation and hydrogenation. For (a) CoRu/TiO_x@AO and (b) CoRu/SmO_x@AO catalysts, the figure shows the Fourier transform infrared (FTIR) spectra, in the region of Co carbonyl species, after 4 h under in situ CO hydrogenation (full, black line). The figure includes also the FTIR spectra corresponding to Co-carbonyl species removed from the surface by subsequent evacuation (dashed blue line) or application of H_2 flow (dotted red line) for 60 min at the reaction temperature. Discontinuous lines correspond to difference spectra, to better visualize the position of those bands whose intensity becomes reduced upon the different postreaction treatments.

after 4 h under reaction for catalysts supported on TiO_x@AO and SmO_x@AO, along with the spectra (determined by subtraction) for those species which are removed from the surface after exposing the catalyst to either vacuum or a flow of H_2 at the reaction temperature. For CoRu/TiO_x@AO, CO molecules adsorbed in a bridged configuration (1865 cm^{-1}) as well as those linearly bonded on Co facets (2045 cm^{-1}) desorbed readily from the catalyst surface upon either cell

DOI: 10.1021/acscatal.5b00057
ACS Catal. 2015, 5, 3323−3335

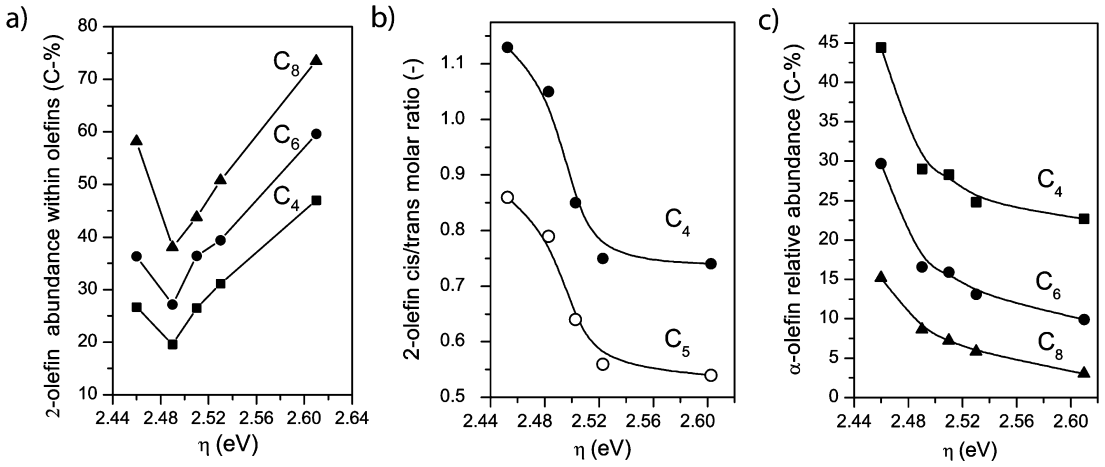

Figure 6. Dependence of (a) the 2-olefin relative molar abundance within the olefin fraction in the C_4, C_6, and C_8 hydrocarbon fractions, (b) the cis/trans 2-olefin isomer ratio in the C_4 and C_5 hydrocarbon fractions, and (c) the α-olefin relative molar abundance in the C_4, C_6, and C_8 hydrocarbon fractions for the series of CoRu/MO_x@AO catalysts with the acid–base character of the support material, represented by the E(IMCT) value of adsorbed alizarin (η). Reaction conditions: T = 493 K, P = 20 bar, CO conversion 40 ± 5%. Data for CoRu/SmO_x@AO have not been included, as the lower intrinsic activity of this catalyst prevented achieving the mentioned CO conversion level.

evacuation or H_2 flow, which indicates that they are weakly adsorbed and hence less likely to be involved in catalysis. However, CO molecules adsorbed on low-coordination sites (band at 2010 cm^{-1}) were only removed under H_2, which indicates that, although more strongly bonded to the metal surface, they are most susceptible to hydrogenation. This observation points to cus sites to be involved in CO hydrogenation, in line with quantum-mechanics predictions of the superior activity of step-edge metal sites.[56] In marked contrast, for CoRu/SmO_x@AO, none of the carbonyl bands underwent any noticeable modification after 1 h exposure to a hydrogen flow (Figure 5b). In this case it is concluded that CO binds strongly to the metallic surface, as indeed was derived from the lower vibration frequencies, while the CO hydrogenation capacity is significantly reduced.

Altogether, our in situ FTIR studies suggest that the differences observed in the reactivity of similarly sized Co nanoparticles supported on oxides of different chemical nature are connected to the presence of support species on the surface of the metal nanoparticles. No significant migration of species from the support on the surface of the Co nanoparticles was concluded for oxides with intermediate acid–base character (Al_2O_3, TiO_x@AO), for which therefore the observed catalytic activity is most representative of the inherent behavior of neat cobalt nanocrystals (TOF ≈ (6–7) × 10^{-2} s^{-1} at 493 K). In the case of a strong Lewis acid oxide such as WO_x@AO, partial reduction during catalyst activation and migration of oxide patches (SMSI) on the cobalt nanoparticles was inferred. The decorating oxide species cover a significant fraction of the cobalt surface, including terraces. Even though such surface blockage reduces the CTY, those Co atoms which remained available for catalysis showed the highest intrinsic CO hydrogenation activity, likely due to the known capacity of partially reduced oxide domains to act as a reservoir of activated hydrogen species and promote spillover to the vicinal metal sites.[57] In contrast, for a support oxide of marked basic character such as SmO_x@AO, few atoms coming from the support oxide are concluded to exist on the cobalt nanoparticles, interacting preferentially with defect sites such as step-edges. Despite the inferred low density of decorating support atoms, they significantly decrease the CO hydrogenation capacity of the catalyst. Such "site-selective blockage" is concluded to be responsible for the decrease in the overall TOF observed under FTS conditions with an increase in the basic character of the oxide support: i.e., decreasing η (Figure 3a).

Insight into the Different Hydrocarbon Selectivities. Deviations from the ideal Anderson–Schulz–Flory (ASF)[58] product distribution are often observed for Co-based catalysts. These commonly include higher CH_4 and lower C_2 hydrocarbon selectivities in comparison to those predicted by the model.[59] In addition, increments in the chain-growth probability with an increase in the hydrocarbon chain have been reported and ascribed to secondary reactions undergone by primary products. In particular, α-olefins, major primary products of the reaction, might readsorb on metal sites and further participate in chain-growth processes (chain reinsertion), contributing to selectivities toward the long-chain product fractions higher than those predicted by the ASF model.[60−62] Although the magnitude of the impact of α-olefin reinsertion on the ultimate selectivity remains debated, there is evidence of its contribution to deviations from the ASF model, particularly noticeable for chain lengths beyond 8–10 carbon atoms, for catalyst particles >100 μm under industrially relevant reaction conditions.[31] Alternatively, α-olefins can also undergo secondary hydrogenation, leading to the corresponding paraffin end products, or double-bond migration and skeletal isomerization reactions, which prevent their effective participation as chain-growth initiators.[63] Under steady reaction conditions, the probability of α-olefins of a given chain length to undergo secondary reactions depends on the number and reactivity of the active sites involved as well as their retention time within the catalyst particles. In this study, contributions from diffusion processes to the observed selectivity differences can be neglected, as the catalyst particle size and the support porosity are kept constant within the series of materials investigated.

The impact of the acid–base character of the support material on the steady-state olefin product distribution is summarized in Figure 6. Primarily, *n*-paraffins, α-olefins, and 2-olefins were detected in the product stream under the applied reaction conditions. The fraction of *iso*-olefins was <1% in all cases, indicating that contributions from skeletal olefin

DOI: 10.1021/acscatal.5b00057
ACS Catal. 2015, 5, 3323–3335

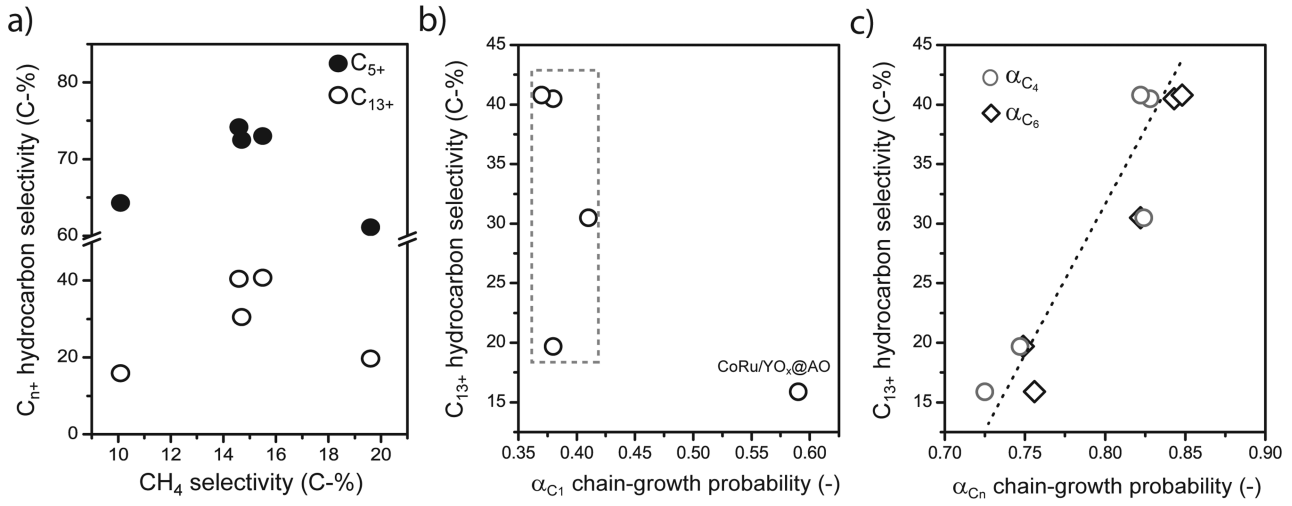

Figure 7. (a) Relationship between the selectivity to long-chain hydrocarbons (C_{5+}, filled symbols; C_{13+}, open symbols) and the selectivity to methane. (b, c) Variation of the selectivity to C_{13+} hydrocarbons with the chain-growth probability for C^*_1 (b) and C^*_{4-6} (c) species for the series of CoRu/MO_x@AO catalysts under steady operation conditions. Reaction conditions: T = 493 K, P = 20 bar, CO conversion 40 ± 5%. Data for CoRu/SmO_x@AO have not been included, as the lower intrinsic activity of this catalyst prevented achieving the mentioned CO conversion level.

isomerization were negligible. For hydrocarbon products with different chain lengths, Figure 6a depicts the relative abundance of 2-olefins, within the olefin fraction, as a function of the η parameter for the oxide support. Invariably for all chain lengths, the molar fraction of 2-olefins passed through a minimum at an intermediate η value of 2.49 eV (Al_2O_3 support), increasing for catalysts supported on oxides with either stronger basic or stronger acidic character. Olefin double-bond migration reactions might be catalyzed by metallic sites[64] as well as acid[65] and basic[66] sites of the oxide support. In this case, a clear signature that the kinetics of α-olefin double-bond shift is governed by the acid−base character of the MO_x species is revealed on analysis of the stereoisomerism of the 2-olefin fraction as a function of the η descriptor. As shown in Figure 6b, the 2-butene cis/trans molar ratio decreased progressively upon an increase in the acidity of the MO_x support oxide, to reach a plateau for η > 2.52 eV. This plateau is in fair agreement with a cis/trans 2-butene ratio of 0.67 calculated in the equilibrium at 493 K[67] and therefore represents a thermodynamic boundary. An analogous trend was observed, though at lower cis/trans ratio values, for C_5 products. These observations are coherent with the double-bond migration reaction proceeding predominately via a carbanion intermediate, which is more stable in the cis conformation, after abstraction of an allylic H on basic sites,[66] i.e. on oxides with low η, but through a carbocation transition state, which favors trans isomers, on acidic sites,[65] such as those predominating on oxides with higher η values. As shown in Figure 6a, oxide supports of intermediate acid−base character most effectively limit the extent to which α-olefin primary products undergo double-bond isomerization.

The α-olefin abundance within the total hydrocarbons showed also a marked dependence on the acid−base character of the oxide support (Figure 6c). For any chain length (C_4−C_8), the proportion of α-olefins decreased continuously on increasing η. Such depletion of α-olefin products for catalysts based on the most acidic oxide supports concurs with their increased activity toward olefin double-bond migration. However, the fact that the α-olefin abundance in the products increased continuously on decreasing η throughout the entire series, also for η values smaller than 2.49 eV (corresponding to the valley observed in Figure 6a), showed that the α-olefin content in the products was not solely determined by their probability of undergoing double-bond migration. The extent to which α-olefins underwent other reactions such as chain reinsertion and/or hydrogenation depended also on the nature of the oxide support.

As a means of understanding the relevance of primary (FTS-related) and secondary reactions to the observed differences in hydrocarbon selectivity—in particular to the targeted C_{13+} fraction—product patterns were analyzed in detail. As depicted in Figure 7a, the selectivities to methane and to long-chain hydrocarbons did not exhibit a correlated variation, which suggests that methane production is kinetically decoupled from the formation of higher hydrocarbons.

In Figures 7b,c, the selectivity to C_{13+} hydrocarbons is plotted against the growth probability parameter for C_n* surface species of different chain length (n). Most catalysts displayed a rather constant value for α_{C1} (ca. 0.39), despite showing notably different C_{13+} selectivities spanning a range of 20−42% (framed region in Figure 7b). Therefore, for this set of catalysts, the selectivity to long-chain hydrocarbons does not relate to the probability with which C_1* monomers undergo chain propagation. As the single outlier in Figure 7b, CoRu/YO_x@AO showed an appreciably higher α_{C1} value of 0.59, pointing to a higher reactivity of the C_1* species toward propagation in this catalyst. When the C_{13+} selectivity was plotted against the growth probabilities for C_n* with four or six carbon atoms, however, a general linear correlation was found involving all catalysts (Figure 7c), as previously reported by others for C_{5+} selectivities.[68] Similar trends were observed if other C^*_{3-10} species were considered (not shown). These results show the propagation probability for C_{2+} species to be determinant for the ultimate C_{13+} selectivity.

The same kinetic descriptors were analyzed as a function of the nature of the oxide support (Figure 8). All catalysts with η ≥ 2.49 eV showed a constant α_{C1} value of 0.39 ± 0.02, notably lower than the corresponding growth probabilities determined for longer hydrocarbon species (Figure 8a). For a more alkaline support such as YO_x@AO (η = 2.46 eV), however, a higher α_{C1}

DOI: 10.1021/acscatal.5b00057
ACS Catal. 2015, 5, 3323−3335

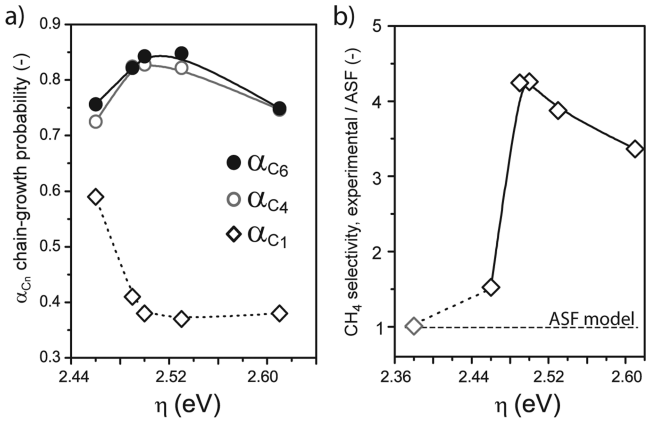

Figure 8. Evolution of (a) the chain-growth probability for C*$_n$ species and (b) the ratio between the experimental CH_4 selectivity and that expected on the basis of the Anderson−Schulz−Flory distribution determined for hydrocarbons with 3−10 carbon atoms as a function of the acid−base character of the support material, represented by the E(IMCT) value of adsorbed alizarin (η). Reaction conditions: T = 493 K, P = 20 bar, CO conversion 40 ± 5%. The gray data point in (b) corresponds to the CoRu/SmO_x@AO catalyst at a CO conversion level of 8%.

value of 0.59 was determined, approaching the growth probabilities of C_{2+}* species for the same catalyst. As a result, the experimental CH_4 selectivity was only ca. 50% higher than that expected from the ideal ASF distribution for this catalyst, whereas methane production was 3−4-fold higher than that predicted by the ASF model for catalysts supported on oxides with higher acidic character ($\eta \geq 2.49$ eV) (Figure 8b). A consistent trend was observed for CoRu/SmO_x@AO, albeit at a lower CO conversion level. For this catalyst, synthesized on the oxide support with the strongest alkaline character of the entire series (η = 2.38 eV), the methane selectivity matched (within ±2%) that predicted by the ASF model. Therefore, on increasing the basicity of the oxide support, the selectivity to CH_4 becomes aligned with that predicted by the ASF model, which concurs with the decreased hydrogenation capacity observed with in situ CO-FTIR for CoRu/SmO_x@AO.

As depicted in Figure 8a for C_4 and C_6, the chain-growth probability for C_{3-10} hydrocarbons showed a volcano dependence with the acid−base nature of the support oxide, being maximum for intermediate values of η. For C_{2+} hydrocarbons, the measured chain growth probabilities might have contributions from both the intrinsic FTS kinetics and secondary α-olefin reinsertion reactions. If the latter play a role, an increment in α_{C_n} with increasing n is expected, resulting in a positive deviation from linearity in an ASF plot.[28,31]

Figure 9a shows the evolution of the chain-growth probability with the hydrocarbon chain length in the C_1−C_{25} range for the set of investigated catalysts, arranged on the basis of the η parameter. In all cases, the highest chain-growth probability occurred for C_2, as is well-known for Co-based FTS catalysts. For longer chains, CoRu/YO_x@AO showed the lowest chain-growth probability of the series (0.71−0.76), rather invariant with the chain length. This translated into a rather straight ASF plot for n > 2 (Figure 9b), i.e. the entire product distribution can be adequately described with a single α value, discarding any significant contribution from α-olefin readsorption to chain growth.

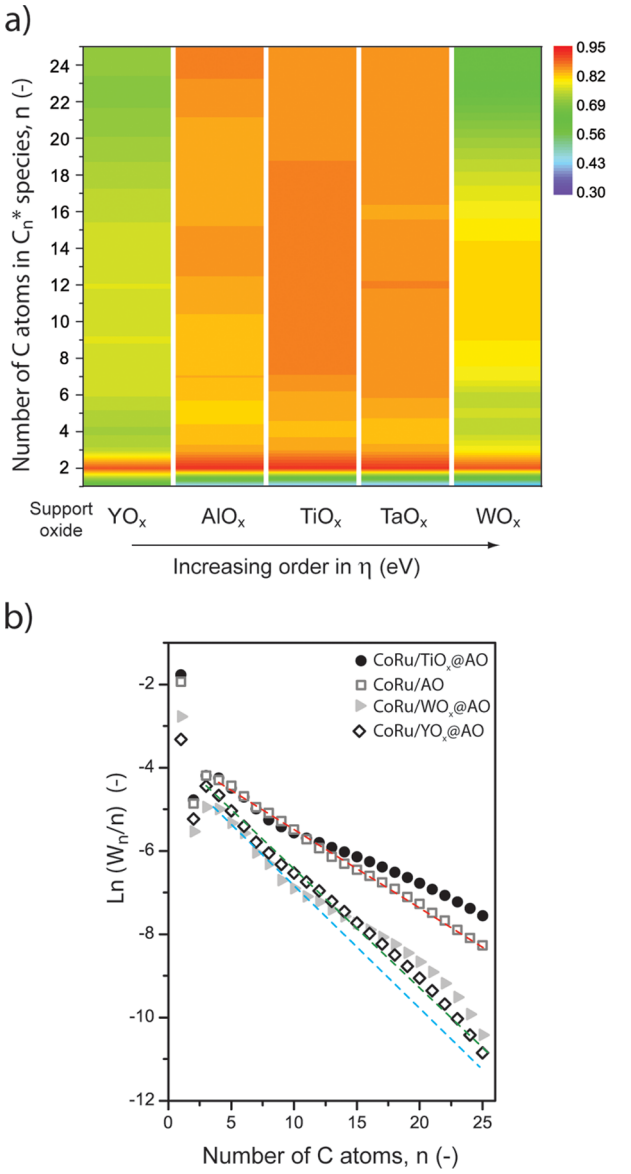

Figure 9. (a) Contour plot of α_{C_n} chain-growth probabilities for hydrocarbon species (n = 1−25) as a function of the acid−base character of the support material, represented by the E(IMCT) value of adsorbed alizarin (η). (b) Experimental Anderson−Schulz−Flory plots for selected CoRu/MO_x@AO catalysts. Symbols correspond to experimental data, while dashed straight lines are guides to the eyes corresponding to the extrapolation of the ASF in the n = 3−8 range, to help visualize how changes in the monotony of the plot are registered for n > 8 for certain catalysts (blue line for CoRu/WO_x@AO, green for CoRu/YO_x@AO, and red for CoRu/AO and CoRu/TiO_x@AO). For clarity, data for CoRu/TaO_x@AO have not been included in (b).

Higher C_{2+} growth probabilities of 0.81−0.92 were observed for catalysts supported on oxides with intermediate acid−base character (Al_2O_3 through TaO_x@AO). Nonetheless, notable differences were also observed among them with regards to the evolution of α_{C_n} with the hydrocarbon chain length. For CoRu/AO, the chain propagation probability remained rather constant throughout the entire range of n = 3−25, as also perceived in the linearity of the corresponding ASF plot (Figure 9b). In contrast, a noticeable increment in the chain growth parameter for n > 8 was observed in the case of CoRu/TaO_x@AO and, most notably, CoRu/TiO_x@AO (Figure 9a). Correspondingly,

DOI: 10.1021/acscatal.5b00057
ACS Catal. 2015, 5, 3323−3335

a positive deviation from the linear behavior was clear in the ASF plot (Figure 9b). Such observations strongly suggest a contribution of α-olefin reinsertion to the overall chain growth mechanism. Similar signs were also observed for CoRu/WO_x@AO. Even though this catalyst showed a lower chain growth probability of ca. 0.79 in the short-chain range (n = 3−7), this parameter increased for n > 8, again suggestive of a secondary contribution from α-olefin reinsertion. However, in contrast to the case of CoRu/TiO_x@AO, α_{C_n} progressively decayed again for n > 15, to reach, for a chain length of 25 carbon atoms, an effective chain growth probability similar to that determined in the n = 3−7 range, which is more indicative of the primary FTS mechanism. In the classical ASF plot, this is observed as a reconvergence of the experimental data to the linear ASF extrapolation for longer hydrocarbon chains (Figure 9b). For this catalyst, it is thus concluded that α-olefin reinsertion contributed to the overall chain growth only up to a limited chain length. For increasingly longer products, the highest activity of this remarkably acidic oxide support toward olefin double-bond isomerization reactions hampers their efficient participation in chain reinsertion processes. Overall, our results prove a significant influence of the acid−base nature of the oxide support on the hydrocarbon product distribution through an interplay of both primary (intrinsic chain growth probability) and secondary phenomena: i.e., α-olefin reinsertion. An oxide support with an intermediate η parameter represents a balance between these factors, which explains why a catalyst supported on TiO_x@AO provides the highest overall chain-growth probability and thereby a remarkably high selectivity to the C_{13+} hydrocarbon fraction.

CONCLUSIONS

Coating a high-surface-area γ-Al_2O_3 carrier with a monolayer content of various metal and lanthanide oxides produces support materials with virtually identical porosities and vastly different surface acid−base characters. Further, incorporation of Co (and Ru promoter) via impregnation and calcination results in highly reducible, model Fischer−Tropsch catalysts with similarly sized Co nanoparticles in the range of >10 nm, where no particle size effects in catalysis are expected. Such a set of model catalysts represents a convenient platform to address intrinsic support effects. Under industrially relevant reaction conditions, the initial TOF (per surface Co^0 atom) increases with an increase in the acidity of the oxide support, as represented by a single spectroscopic parameter of the Lewis acid−base character. However, the overall reaction rate (cobalt time yield) reaches a maximum for oxide supports of intermediate acid−base character. Such volcano dependence of the metal-specific activity with the nature of the support is due to the interplay between both the number of surface-exposed cobalt sites and their intrinsic activity. For alkaline oxide supports, i.e. lanthanide oxides, few lanthanide atoms are inferred on the surface of the Co nanoparticles after reduction, which strengthens CO adsorption and significantly decreases CO hydrogenation, likely via a "selective blockage" of few cobalt sites, possibly step-edges, which are nevertheless essential for CO hydrogenation. In contrast, "unselective site-blockage" via decoration of Co nanoparticles with oxide patches (strong metal−support interaction) is concluded for stronger Lewis acid, more reducible oxide supports, particularly WO_x. This causes a decrease in the number of Co sites available for catalysis. Next to the activity, the acid−base nature of the oxide support also controls the nature and extent of secondary reactions of the α-olefin products and the overall selectivity to long-chain products. The selectivity to the relevant C_{13+} hydrocarbon fraction shows a volcano-type evolution with the acid−base character of the support. Such dependence is the result of the interplay between both intrinsic parameters, associated with the primary Fischer−Tropsch mechanism, and secondary processes, likely α-olefin reinsertion, which in both cases depend on the chemical nature of the oxide support. As they have an adequate balance between these factors, Co nanoparticles supported on TiO_x-coated Al_2O_3 unite an optimum activity and selectivity, resulting in an outstanding cobalt time yield and C_{13+} productivity. The insights obtained for this set of model catalysts contribute toward a general view of the support effects in cobalt Fischer−Tropsch catalysts over a broad study space and should therefore serve to guide the development of advanced catalysts.

ASSOCIATED CONTENT

Supporting Information

The Supporting Information is available free of charge on the ACS Publications website at DOI: 10.1021/acscatal.5b00057.

X-ray diffraction patterns for support materials, relationship between surface acidity of MO_x@AO supports and the theoretical (Lewis) acidity of the corresponding M_yO_z bulk oxides, supporting XPS data and analysis, UV−vis spectra of support materials prior to and after alizarin adsorption, comparison of CTY for CoRu/TiO_x@Al_2O_3 with literature data, dependence of the productivity to C_{13+} hydrocarbons with the acid−base character of the oxide support, summary of the hydrocarbon selectivities obtained in the FTS experiments (PDF)

AUTHOR INFORMATION

Corresponding Authors

*E-mail for G.P.: prieto@kofo.mpg.de.
*E-mail for A.M.: amart@itq.upv.es.

Present Address

§(G.P.) Max Planck Institut für Kohlenforschung, Kaiser-Wilhelm-Platz 1, D 45470 Mülheim an der Ruhr, Germany.

Notes

The authors declare no competing financial interest.

ACKNOWLEDGMENTS

The authors are grateful to Sasol for providing the high-purity pseudoboehmite sample and to the Microscopy Service of the UPV for specimen preparations. This work has been funded by the Spanish Government-MINECO through "Severo Ochoa" (SEV 2012-0267) and Consolider Ingenio 2010-Multicat projects.

REFERENCES

(1) Dry, M. E. *Catal. Today* **2002**, *71*, 227−241.
(2) Wood, D. A.; Nwaoha, C.; Towler, B. F. *J. Nat. Gas Sci. Eng.* **2012**, *9*, 196−208.
(3) van Steen, E.; Claeys, M. *Chem. Eng. Technol.* **2008**, *31*, 655−666.
(4) Jahangiri, H.; Bennett, J.; Mahjoubi, P.; Wilson, K.; Gu, S. *Catal. Sci. Technol.* **2014**, *4*, 2210−2229.
(5) Khodakov, A. Y.; Chu, W.; Fongarland, P. *Chem. Rev.* **2007**, *107*, 1692−1744.

DOI: 10.1021/acscatal.5b00057
ACS Catal. 2015, 5, 3323−3335

(6) Zhang, Q.; Kang, J.; Wang, Y. *ChemCatChem* **2010**, *2*, 1030−1058.
(7) de Klerk, A. In *Fischer−Tropsch Refining*; Wiley-VCH: Weinheim, Germany, 2011.
(8) Bezemer, G. L.; Bitter, J. H.; Kuipers, H. P.; Oosterbeek, H.; Holewijn, J. E.; Xu, X.; Kapteijn, F.; van Dillen, A. J.; de Jong, K. P. *J. Am. Chem. Soc.* **2006**, *128*, 3956−3964.
(9) Prieto, G.; Martínez, A.; Concepción, P.; Moreno-Tost, R. *J. Catal.* **2009**, *266*, 129−144.
(10) Fischer, N.; van Steen, E.; Claeys, M. *J. Catal.* **2013**, *299*, 67−80.
(11) Tuxen, A.; Carenco, S.; Chintapalli, M.; Chuang, C.-H.; Escudero, C.; Pach, E.; Jiang, P.; Borondics, F.; Beberwyck, B. J.; Alivisatos, A. P.; Thornton, G.; Pong, W.-F.; Guo, J.; Perez, R.; Besenbacher, F.; Salmeron, M. *J. Am. Chem. Soc.* **2013**, *135*, 2273−2278.
(12) Karaca, H.; Safonova, O. V.; Chambrey, S.; Fongarland, P.; Roussel, P.; Griboval-Constant, Z.; Lacroix, M.; Khodakov, A. Y. *J. Catal.* **2011**, *277*, 14−26.
(13) Liu, J.-X.; Su, H.-Y.; Sun, D.-P.; Zhang, B.-Y.; Li, W.-X. *J. Am. Chem. Soc.* **2013**, *135*, 16284−16287.
(14) Prieto, G.; Concepción, P.; Murciano, R.; Martínez, A. *J. Catal.* **2013**, *302*, 37−48.
(15) Jermwongratanachai, T.; Jacobs, G.; Shafer, W. D.; Pendyala, V. R. R.; Ma, W.; Gnanamani, M. K.; Hopps, S.; Thomas, G. A.; Kitiyanan, B.; Khalid, S.; Davis, B. H. *Catal. Today* **2014**, *228*, 15−21.
(16) Morales, F.; Weckhuysen, B. M. In *Catalysis*; Spivey, J. J., Dooley, K. M., Eds.; The Royal Society of Chemistry: Cambridge, U.K., 2006; Vol. *19*, pp 1−40.
(17) Cook, K. M.; Poudyal, S.; Miller, J. T.; Bartholomew, C. H.; Hecker, W. C. *Appl. Catal., A* **2012**, *449*, 69−80.
(18) Di Fronzo, A.; Pirola, C.; Comazzi, A.; Galli, F.; Bianchi, C. L.; Di Michele, A.; Vivani, R.; Nocchetti, M.; Bastianini, M.; Boffito, D. C. *Fuel* **2014**, *119*, 62−69.
(19) Concepción, P.; López, C.; Martínez, A.; Puntes, V. F. *J. Catal.* **2004**, *228*, 321−332.
(20) Sartipi, S.; Parashar, K.; Valero-Romero, M. J.; Santos, V. P.; van der Linden, B.; Makkee, M.; Kapteijn, F.; Gascon, J. *J. Catal.* **2013**, *305*, 179−190.
(21) Kim, J.-C.; Lee, S.; Cho, K.; Na, K.; Lee, C.; Ryoo, R. *ACS Catal.* **2014**, *4*, 3919−3927.
(22) Liu, Y.; de Tymowski, B.; Florea, I.; Ersen, O.; Meny, Ch.; Nguyen, P.; Pham, Ch.; Luck, F.; Pham-Huu, C. *ACS Catal.* **2013**, *3*, 393−404.
(23) Xiong, H.; Motchelaho, M. A. M.; Moyo, M.; Jewell, L. L.; Coville, N. J. *J. Catal.* **2011**, *278*, 26−40.
(24) Liu, P. S.; Chen, G. F. In *Porous Materials: Processing and Applications*, 1st ed.; Butterworth-Heinemann Elsevier: Oxford, U.K., 2014.
(25) Reuel, R. C.; Bartholomew, C. H. *J. Catal.* **1984**, *85*, 78−88.
(26) Borg, Ø.; Dietzel, P. D. C.; Spjelkavik, A. I.; Tveten, E. Z.; Walmsley, J. C.; Diplas, S.; Eri, S.; Holmen, A.; Rytter, E. *J. Catal.* **2008**, *259*, 161−164.
(27) Schmal, M.; Aranda, D. A. G.; Soares, R. R.; Noronha, F. B.; Frydman, A. *Catal. Today* **2000**, *57*, 169−176.
(28) Iglesia, E. *Appl. Catal., A* **1997**, *161*, 59−78.
(29) Takahashi, N.; Mori, T.; Miyamoto, A.; Hattori, T.; Murakami, Y. *Appl. Catal.* **1988**, *38*, 61−69.
(30) Bertole, C. J.; Mims, C. A.; Kiss, G. *J. Catal.* **2004**, *221*, 191−203.
(31) Iglesia, E.; Reyes, S. C.; Madon, R. J. *J. Catal.* **1991**, *129*, 238−256.
(32) Zhang, Y.; Yoneyama, Y.; Tsubaki, N. *Chem. Commun.* **2002**, 1216−1217.
(33) Martinez, A.; Prieto, G.; Rollán, J. *J. Catal.* **2009**, *263*, 292−305.
(34) Khodakov, A. Y.; Griboval-Constant, A.; Bechara, R.; Zholobenko, V. L. *J. Catal.* **2002**, *206*, 230−241.
(35) Prieto, G.; Concepción, P.; Martínez, A.; Mendoza, E. *J. Catal.* **2011**, *280*, 274−288.
(36) Jeong, N. C.; Lee, J. S.; Tae, E. L.; Lee, Y. J.; Yoon, K. B. *Angew. Chem., Int. Ed.* **2008**, *47*, 10128−10132.
(37) Reuel, R. C.; Bartholomew, C. H. *J. Catal.* **1984**, *85*, 63−77.
(38) Iglesia, E.; Soled, S. L.; Fiato, R. A. *J. Catal.* **1992**, *137*, 212−224.
(39) Kerkhof, F. P. J. M.; Moulijn, J. A. *J. Phys. Chem.* **1979**, *83*, 1612−1619.
(40) Saib, A. M.; Moodley, D. J.; Ciobîca, I. M.; Hauman, M. M.; Sigwebela, B. H.; Weststrate, C. J.; Niemantsverdriet, J. W.; van de Loosdrecht, J. *Catal. Today* **2010**, *154*, 271−282.
(41) Prieto, G.; Meeldijk, J. D.; de Jong, K. P.; de Jongh, P. E. *J. Catal.* **2013**, *303*, 31−40.
(42) Soled, S. L.; Iglesia, E.; Fiato, R. A.; Baumgartner, J. E.; Vroman, H.; Miseo, S. *Top. Catal.* **2003**, *26*, 101−109.
(43) Maitlis, P. M.; Zanotti, V. *Chem. Commun.* **2009**, 1619−1634.
(44) Vannice, M. A. *Catal. Today* **1992**, *12*, 255−267.
(45) Boffa, A. B.; Lin, C.; Bell, A. T.; Somorjai, G. A. *J. Catal.* **1994**, *149*, 149−158.
(46) Iglesia, E.; Soled, S. L.; Fiato, R. A.; Via, G. H. *J. Catal.* **1993**, *143*, 345−368.
(47) Eschemann, T. O.; Bitter, J. H.; de Jong, K. P. *Catal. Today* **2014**, *228*, 89−95.
(48) Song, D.; Li, J.; Cai, Q. *J. Phys. Chem. C* **2007**, *111*, 18970−18979.
(49) Couble, J.; Bianchi, D. *J. Phys. Chem. C* **2013**, *117*, 14544−14557.
(50) Blyholder, G. J. *J. Phys. Chem.* **1964**, *68*, 2772−2777.
(51) Bönicke, I. A.; Thieme, F.; Kirstein, W. *Surf. Sci.* **1998**, *395*, 138−147.
(52) Norris, A. G.; McGrath, R. *J. Phys.: Condens. Matter* **1999**, *11*, 9549−9554.
(53) Blyholder, G.; Lawless, M. *Langmuir* **1991**, *7*, 140−141.
(54) Ojeda, M.; Nabar, R.; Nilekar, A. U.; Ishikawa, A.; Mavrikakis, M.; Iglesia, E. *J. Catal.* **2010**, *272*, 287−297.
(55) Shetty, S.; van Santen, R. A. *Catal. Today* **2011**, *171*, 168−173.
(56) van Santen, R. A.; Ghouri, M. M.; Shetty, S.; Hensen, E. M. H. *Catal. Sci. Technol.* **2011**, *1*, 891−911.
(57) Conner, W. C.; Falconer, J. L. *Chem. Rev.* **1995**, *95*, 759−788.
(58) Friedel, R. A.; Anderson, R. B. *J. Am. Chem. Soc.* **1950**, *72*, 2307−2307.
(59) Jacobs, G.; Davis, B. H. *Catal. Sci. Technol.* **2014**, *4*, 3927−3944.
(60) Smith, D. F.; Hawk, C. O.; Golden, P. L. *J. Am. Chem. Soc.* **1930**, *52*, 3221−3232.
(61) Kuipers, E. W.; Scheper, C.; Wilson, J. H.; Vinkenburg, I. H.; Oosterbeek, H. *J. Catal.* **1996**, *158*, 288−300.
(62) Schulz, H.; Claeys, M. *Appl. Catal., A* **1999**, *186*, 71−90.
(63) Schulz, H. *Top. Catal.* **2003**, *26*, 73−85.
(64) Twigg, G. H. *Trans. Faraday Soc.* **1939**, *35*, 934−940.
(65) Brouwer, D. M. *J. Catal.* **1962**, *1*, 22−31.
(66) Hattori, H. *Chem. Rev.* **1995**, *95*, 537−558.
(67) Equilibrium cis/trans 2-butene composition as simulated with Aspen Plus using an RGibbs reactor at T = 493 K and P = 1 atm and the predictive Soave−Redlich−Kwong (PSRK) group-contribution equation of state.
(68) Lögdberg, S.; Lualdi, M.; Järås, S.; Walmsley, J. C.; Blekkan, E. A.; Rytter, E.; Holmen, A. *J. Catal.* **2010**, *274*, 84−98.

DOI: 10.1021/acscatal.5b00057
ACS Catal. 2015, 5, 3323−3335